The role of refractive indices in measuring mineral dust with high-spectral resolution infrared satellite sounders: Application to the Gobi Desert

Perla Alalam[1], Fabrice Ducos[1], Hervé Herbin[1]

5   [1]Laboratoire d'Optique Atmosphérique, LOA, UMR 8518, CNRS, Université de Lille, F-59000 Lille, France

Correspondence to: Hervé Herbin (heve.herbin@univ-lille.fr)

Abstract. Mineral dust significantly influences the Earth's climate system by affecting the Earth's radiative balance through the absorption and scattering of solar and terrestrial radiation. Understanding the physico-chemical properties of dust in the longwave region of the electromagnetic spectrum is crucial for a more accurate estimation of the radiative budget. The complex refractive

10   index (CRI) of dust in the infrared (IR) is a key parameter for mineral dust characterization from satellite remote sensing. Particularly, high-spectral-resolution instruments have shown the ability to measure these aerosol properties, e.g., the Infrared Atmospheric Sounding Instrument (IASI). This work reviews six prior laboratory Complex Refractive Index (CRI) datasets, which focus on advancements in laboratory measurement techniques aimed at characterizing dust properties via IASI measurements during a dust storm event over the Gobi Desert in May 2017. We evaluate the sensitivity of IASI to different CRI datasets using

15   the ARAHMIS radiative transfer algorithm and explore their impact on retrieving size distribution parameters by mapping their spatial distribution. The results indicate that the new laboratory CRI datasets decrease the total error by 30% and that the choice of CRI significantly impacts the accuracy of dust detection and characterization from satellite observations. Notably, datasets that incorporate aerosol generation techniques with higher spectral resolution and samples from the case study region show enhanced compatibility with IASI observations. The outcomes of this research emphasize two key points: the crucial connection between

20   dust's chemical composition and its optical properties, and the need to consider the specific composition of the CRI dataset for improved retrieval of the microphysical parameters. Moreover, this study highlights the critical role of continuous enhancements in CRI measurement approaches, as well as the potential of high-spectral-resolution infrared sounders for aerosol atmospheric investigation and understanding their radiative impacts.

1 Introduction

25   Mineral dust, carried by strong winds from arid regions into the atmosphere, interacts with solar and terrestrial radiation, significantly impacting Earth's radiative budget (Kok et al., 2017). To date, estimating the aerosol radiative effect presents considerable uncertainties, as highlighted in reports by the Intergovernmental Panel on Climate Change (IPCC). These uncertainties primarily arise from the lack of detailed knowledge about the physicochemical properties of mineral dust, which exhibit significant spatial and temporal variations (Masmoudi et al., 2003; Journet et al., 2014). The size distribution of dust

30   particles ranges from hundreds of nanometers to tens of micrometers, with the mineral composition varying according to the dust's source region. This diversity allows remote sensing instruments to detect mineral dust by capturing spectral signatures in the ultraviolet (UV), visible (Vis), and infrared (IR) spectral ranges. Notably, satellite sensors offer a comprehensive perspective on the mineral dust cycle, encompassing its emission, transport, and deposition, and spanning from regional to global scales. Consequently, radiative transfer models have been developed to simulate spectral fits based on actual satellite observations,

35   incorporating valuable data on the physicochemical and optical properties of dust particles. The most recognized retrievals are

conducted in the visible spectrum (e.g., the GRASP algorithm), enabling precise measurements of the Aerosol Optical Depth (AOD) and the derivation of aerosol parameters from satellite instruments such as the POLarization and Directionality of the Earth's Reflectances (POLDER) (Dubovik et al., 2011).

40 More recently, IR instruments have made significant contributions to the detection of mineral dust due to their high sensitivity to the particles' composition. They offer the advantage of distinguishing the vibrational modes of various minerals and excel in nighttime detections (Sokolik et al., 1998; Ryder et al., 2019). For example, high-spectral-resolution satellite sounders, such as the Infrared Atmospheric Sounding Instrument (IASI), exploit the spectral variations of dust in the thermal IR range (750 - 1250 cm^{-1}) to quantify their physicochemical properties of dust using radiative transfer algorithms (Clarisse et al., 2010; Klüser et al., 2015; Capelle et al., 2018). Nevertheless, significant uncertainties persist in IR radiative transfer retrievals from satellite observations,

45 primarily due to our limited knowledge of the complex refractive index (CRI) of mineral dust. The CRI links the particles' optical properties, characterized by absorption and scattering processes, to their chemical composition or mineralogy, which vary from one source to another.

One of the earliest datasets for CRI applied to mineral dust originated from Peterson and Weinman, 1969 and focused on pure crystalline quartz, a major dust component. They exploited reflectance spectra and dispersion theory of solid crystal that were

50 originally obtained by Spitzer and Kleinman, 1961. In the 1970s, the first natural dust samples, obtained from filtered rainout precipitation and Saharan dust, were processed into glassy disc KBr pellets to measure reflectivity, and subsequently calculate the CRI in the IR spectrum (Volz 1972, 1973).

In the following years, recognizing that mineral dust consists of an aggregate of different minerals such as silicates, clays, carbonates, and iron oxides, various pure mineral CRIs were examined across a spectrum from infrared to ultraviolet using the

55 pellets technique (Querry et al., 1978; Egan and Hilgeman, 1979; Glotch et al., 2007). Balkanski et al., 2007 further refined aerosol radiative forcing assessments in the visible spectrum, employing pure mineral mixtures alongside literature CRIs, yielding more accurate radiative estimates than those by Volz 1972, 1973 . Furthermore, Capelle et al., 2014 highlighted the IASI brightness temperature sensitivity's 25% error in response to refractive index changes, as identified by Balkanski et al., 2007.

From the 2000s, aerosol optical properties research increasingly incorporated advanced experimental techniques. These involved

60 aerosol generation methods more representative of natural airborne dust, in contrast to the pellet/film approach that alters particle size, shape, and vibrational modes. One of the initial systems to combine mineral dust generation with extensive measurement analysis, was established at the University of Iowa, utilizing the Multi-Analysis Aerosol flow Reactor System (MAARS) (Gibson et al., 2006). This setup was specifically used to generate clay mineral aerosols for extinction measurements and particle size distribution analysis, with a focus on examining the sphericity of the particles (Hudson et al., 2007). The Rutherford Appleton

65 Laboratory's Molecular Spectroscopy Facility (RAL-MSF) was also adapted for aerosol generation and high-resolution extinction spectrum measurements, alongside size distribution analysis to study the sphericity and crystallinity of quartz particles and derive the CRI of volcanic ash (Reed et al., 2017, 2018). Moreover, at the University Paris-Est Créteil, the CESAM (Chambre Expérimentale de Simulation Atmosphérique Multiphasique) was employed to generate mineral dust aerosols from various desert soils worldwide. These experiments, conducted under relevant atmospheric conditions, involved measuring extinction and size

70 distribution to obtain CRI (Di Biagio et al., 2017). Finally, at the University of Lille, the PhysicoChimie des Processus de Combustion et de l'Atmosphère (PC2A) platform has been employed for generating samples from the Gobi Desert, pure minerals like quartz, illite, kaolinite and calcite and volcanic ash under dry atmospheric conditions, aiming to measure the extinction coefficient and size distribution and derive the CRI data spanning a wide spectral range from far infrared to UV (Deschutter, 2022; Deguine et al., 2023; Chehab et al., 2024).

75 The objective of this paper is to investigate the influence of the new CRI measurements in comparison to previous datasets on IASI mineral dust retrievals. Firstly, we assess the sensitivity of IASI observations to a range of CRI datasets from literature. This includes a detailed analysis of the information content in these datasets, aiming to understand how variations in CRI measurements influence the IASI's ability to accurately detect and characterize the microphysical dust properties. This step is crucial for identifying the strengths and limitations of current datasets while emphasizing the need for enhancements in CRI measurement

80 techniques. Secondly, we apply the inversion process to a dust event that occurred on 4 May 2017 over the Gobi Desert in East Asia. By focusing on this specific event, we examine the capability of accurately reproducing detections and the extent to which we can retrieve the microphysical properties of dust particles. This analysis also evaluates how the incorporation of new CRI measurements and the mixture methodology from the mineralogical study on East Asia by Alalam et al., 2022 can enhance the accuracy of mineral dust retrievals.

2 Case Study

East Asia is the second largest source of mineral dust after the Sahara, producing up to 800 Tg per year (An et al., 2018). This significant output is primarily associated with strong winds that disperse substantial quantities of mineral dust, particularly during the winter and spring months. An intense dust storm occured from 3 to 8 May 2017, affecting visibility across North China. From the southwest of Inner Mongolia, the dust plume travelled passing through North China, the Korean peninsula, and Japan before

90 dissipating in Russia. Three cold fronts generated dust loads during this event. The first two fronts lifted dust from the Gobi Desert on 3 May. A third front emerged on 4 May, resulting in distinct dust plumes that merged between May 4 and May 6, originating from both the Horqin Sandy Land and the Gobi Desert (Minamoto et al., 2018; Alalam et al., 2022).

In this study, we focus on the 4 May when the dust plume was at its most dispersion and visibility to IASI observations. **Figure 1** illustrates the IASI brightness temperature difference during the Gobi dust storm on the 4 May 2017, during daylight hours. To

95 select IASI dust spectra, we employ the 'V-shape' dust criteria, which involves computing the difference in brightness temperature ($\Delta T_B = T_{B,1191.25} - T_{B,1112}$). The choice of brightness temperature channels is influenced by two key factors: the concentration variability and the narrow absorption bands from gases. As dust concentration increases, the 'V-shape' of the AOD becomes more pronounced, making measurements in the MIR more sensitive to concentration fluctuations (Alalam, 2022). Consequently, the difference in brightness temperature acts as a reliable indicator for determining the AOD.

3 The datasets and methods

3.1 IASI data selection

IASI is an infrared Fourier transform spectrometer that is part of the METOP satellite series, developed by CNES in cooperation with EUMETSAT. Since 2006, two sun-synchronized METOP satellites (B and C) are still in orbit, each with an IASI instrument on board. METOP A was switched off in November 2021, and a new generation of IASI-NG will continue the mission for the next

105 20 years, featuring increased spectral resolution and radiometric performance (Crevoisier et al., 2014). The instrument scans in nadir view with a swath of 2200 km. The field of view corresponds to 2×2 circular pixels, each with a 12 km diameter footprint at nadir. The IASI covers a continuous infrared spectral range between 645 and 2760 cm^{-1} (3.62 and 15.5 μm) providing 8461 channels with a spectral resolution of 0.5 cm^{-1} and low radiometric noise (Blumstein et al., 2004).

The mineral dust spectral selection method, as detailed by Alalam et al., 2022 is briefly summarized here. The input data are taken

110 from IASI-A level 1c and level 2 data from EUMETSAT data center (https://data.eumetsat.int/) and processed using a principal

component analysis (PCA) code developed at the Laboratoire d'Optique Atmosphérique (LOA). The PCA filters spectra into dust, cloud, and clear sky pixel types, with a requirement of 90% of type homogeneity in the IASI pixel. Following this, a land surface emissivity (LSE) method is applied to the radiances to correct the LSE effect. Finally, the selection of the mineral dust spectra is applied under a condition on the difference in brightness temperature.

3.2 The CRI data

In this study, we choose to compare relevant CRI datasets employed in radiative transfer algorithms in the mid-infrared (MIR) spectral range (further references can be found and are listed by Clarisse et al., 2019. The selected CRI datasets are as follows:

1- The first dataset originates from Volz, 1972 (VZ72), where the dust was separated from mid-latitude natural precipitation, including a mixture of soil particles, airborne soot, and pollen. The sample was blended and pressed under vacuum conditions to form a glassy disc using the classical pellet method. The CRI was calculated based on the measured absorption coefficient of the bulk material. It has previously been used in altitude and concentration retrievals from IASI (Vandenbussche et al., 2013; Capelle et al., 2017).

2- Similar measurements were conducted on the second dataset, also from Volz, 1973 (VZ73), with the sample collected from Saharan sand in Barbados. This dataset has been widely utilized in Saharan dust retrievals (Clarisse et al., 2019; Desouza-Machado et al., 2010), as well as IASI dust level 2 products (ULB and LMD algorithms, https://cds.climate.copernicus.eu). Compared to other data from the Sahara, this dataset has shown to be the most representative for long-range transported Saharan dust (Clarisse & Astoreca, 2021).

3- The third dataset is derived from the Optical Properties of Aerosols and Clouds (OPAC) known as "mineral transported," calculated by Hess et al., 1998. It combines data from VZ73 and quartz. It has previously been used for quantifying Saharan and Asian dust (Cuesta et al., 2015; Klüser et al., 2015).

4- The fourth dataset, from Di Biagio et al., 2017 (DB17), represents a more recent measurement of refractive indices and is based on 19 global dust samples, with the soil collected from the Gobi Desert. Aerosols were generated and suspended in the CESAM chamber under atmospheric relevant conditions, and the CRI was retrieved using an optical inversion procedure. A recent study compared the Gobi and the Taklamakan Deserts' refractive indices with Volz in 1972, demonstrating a clear impact on the brightness temperature spectrum simulations in the MIR (Bi et al., 2020). These datasets were used in a climatological analysis of coarse-mode dust over global oceans (Zheng et al., 2023).

5- The fifth dataset, as measured by Deschutter, 2022 (DSC22) at the PC2A platform, also involves aerosols generated from a Gobi Desert dust sample but under dry atmospheric conditions. The CRI was retrieved using an optimal inversion method, and the dataset was previously used by Alalam et al. in 2022 to determine the mineralogical fraction of East Asian dust from IASI spectra.

6- A sixth dataset consists of a mixture of pure minerals (quartz, illite, and calcite), as measured by Deschutter, 2022. We calculated an effective CRI using the Volume Mixing Approximation (VMA) one of the simplest approaches of the effective medium theory. The effective properties of an aggregate of minerals is considered as a weighted average of the properties of its pure minerals' constituents, with the weighting factors being their volume fractions (for a detailed explanation, refer to Sokolik and Toon, 1999). The volume fractions values are 15.3%, 80.0%, 4.7% for quartz, illite and calcite respectively. The percentages were determined based on linear combination calculations by Alalam et al., 2022, using the experimental extinction coefficient of the Gobi sample from which DSC22 was derived.

Figure 2 illustrates the complex refractive indices in the MIR range. Spectral signatures variations are apparent, primarily due to differences in the sampled dust regions, and therefore difference in the mineralogy. The most pronounced contrast in the CRI can

150 be observed for VZ72, which originates from rainout precipitation rather than desert dust. DB17 and DSC22, both sampled from the Gobi Desert, exhibit similar spectral features but with distinct values, indicating that the setup and method used can also influence the derived CRI. On the other hand, OPAC is derived from a mixture of VLZ73 and quartz and has a greater impact on the real index than the imaginary index. Notably, the molecular signatures of quartz are more prominent in the vicinity of 800 and 1100 cm^{-1}.

3.3 The inversion process

155 The inversion process follows the formalism of the optimal estimation method (OEM) described by Rodgers, 2000. This approach allows us to assess the sensitivity of the measurement and its information content, and the separation of parameters derived directly from the measurement and those provided by the a priori state. Furthermore, it enables the calculation of errors arising from measurement noise and the smoothing effect imposed on the actual profile by the observation system, which includes both the
160 instrument measurement and the non-retrieved parameters.

3.3.1 The forward model

To solve the forward transfer equation, we use an analytical relationship that links between the set of observations y (in this case, the IASI radiances), and the state vector x, which its elements consist of the variables to be retrieved, and it is written as:

$$y = F(x, b) + \varepsilon \tag{1}$$

165 where F represents the forward model (here the ARAHMIS code), b correspond to the fixed parameters affecting the measurement (i.e., the atmospheric conditions, gases concentrations, surface emissivity and temperature) and ε is the measurement error vector. In this work, the state vector x elements are:

(1) The geometric size diameter D_g, which follows a lognormal distribution with a fixed geometric standard deviation σ_g. To compare results with literature, we calculate an effective diameter ($D_e = D_g e^{2.5(ln\sigma_g)^2}$) corresponding a fixed geometric
170 standard deviation $\sigma_g = 2.0$ as suggested by Clarisse et al., 2019.

(2) The volume mixing ratio (VMR), which is defined as the ratio of the volume of a dust with respect to the total volume of the air sample. It expressed in parts per million (ppm) providing a standardized way to express the aerosols concentration in the atmosphere.

We chose only these two elements to establish a link between the microphysical properties of dust (size and concentration) and
175 their mineralogical composition identified in Alalam et al., 2022, for the same case study. The forward model is computed using the ARAHMIS line-by-line full physics radiative transfer algorithm, allowing for precise simulations of observed IASI radiances across the MIR, from which we select spectra ranging from 785 to 1235 cm^{-1}. The atmosphere is discretized into layers, each with a 1 km thickness. Gaseous spectroscopic parameters, including spectral line positions, intensities, and half-maximum widths, are computed based on the updated HITRAN 2020 database. The atmospheric conditions, such as pressure, temperature, and water
180 vapor profiles, were derived from the UWYO database at the Dalanzadgad station (http://weather.uwyo.edu/upperair/sounding.html). The ozone profile was obtained from the WOUDC database at the Xhianghe station (https://woudc.org). The CO_2 and CH_4 profiles were taken from the CAMS Greenhouse Gases reanalysis (https://ads.atmosphere.copernicus.eu). Surface temperature data were acquired from the level 2 IASI product provided by EUMETSAT (https://data.eumetsat.int/). Surface emissivity was originally obtained from Zhou et al. in 2014. Nevertheless, it's
185 essential to note that our detections are primarily over land areas. Therefore, we applied a correction factor, employing the method described by Alalam et al., 2022, to ensure appropriate adjustments for surface emissivity in IASI spectral simulations.

For aerosols, we consider the single scattering approximation, which assumes that the distance between aerosol particles is larger than the range of their size distribution. Consequently, the particles are sufficiently spaced such that the scattering of light by one particle occurs independently of others. This assumption is applicable in our case where we select only non-opaque IASI spectra

190 using the PCA code. To calculate the aerosols extinction coefficient $k_{ext}^{aerosols}$, we use a Mie scattering code designed for spherical particles. This approach was previously used in the MIR as it is less sensitive to the shape of particles (Yang et al., 2007; Di Biagio et al., 2017). The particle size distribution is assumed to be monomodal and lognormal, similar to the method described by Pierangelo et al., 2005. This distribution is characterized by the total number of particles N_0, a geometric size diameter D_g and a geometric standard deviation σ_g. The mean layer dust altitude is set at $Z = 2$ km with a thickness of $L = 1$ km. This choice is based

195 on the CALIOP orbit track above the dust plume on May 4, 2017, as illustrated by Alalam et al., 2022.

Figure 3 illustrates a comparison of the extinction coefficient as derived from the six CRI datasets using Mie theory and assuming an effective diameter D_g=1.0 µm. The extinction was normalized to remove the dependency on the concentration. All six datasets exhibit a characteristic signature associated with silicates, the familiar bent observed in the neighbouring of 1050 cm^{-1}. Deguine et al., 2020 highlighted that as the silica fraction increases, the extinction peak values move to higher wavenumbers. DCS22, and

200 VMA are smoother and have more pronounced peaks: similar double peak tectosilicates feature is observed near 778 and 795 cm^{-1}, carbonates peak at 879 cm^{-1} and phyllosilicates peak at 916 cm^{-1}. Notably, the spectral resolution is low in other datasets: in OPAC no double peak features can be distinguished, while VZ72 does not show any discernible peaks between 750 and 980 cm^{-1}, and VZ73 only exhibits a signature near 916 cm^{-1}. This difference may be attributed to the improvement in the experimental measurement in the late years and the chemical composition of the dust source.

205 **3.3.2 Information content analysis**

The information content (IC) analysis enables us to establish the sensitivity of the inversion for each parameter sought, and hence make an optimal selection of those parameters and the constrains applied depending on their sensitivity on the spectrum. This analysis allows to quantify the impact of each parameter on the retrieval accuracy and allows us to gain in computational time and increase the quality of adjustment, by constraining parameters and hence avoid too great correlation between them.

210 Following Herbin et al., 2013, two matrices ($\mathbf{A}$ and $\mathbf{S_x}$) can fully characterize the information provided by IASI and they are needed to perform this analysis.

The averageing Kernel matrix $\mathbf{A}$, gives the sensitivity of the retrieved state to the true state, and is given by:

$$\mathbf{A} = \delta\hat{x}/\delta x = \mathbf{GK} \qquad (2)$$

215 where $\mathbf{K}$ is the Jacobian matrix written by $\mathbf{K} = \delta F/\delta x$, and $\mathbf{G}$ is the gain matrix which rows are the derivatives of the retrieved state with respect to the spectral points, and is written by:

$$\mathbf{G} = \delta\hat{x}/\delta y = (\mathbf{K^T S_\varepsilon^{-1} K} + \mathbf{S_a^{-1}})^{-1}\mathbf{K^T S_\varepsilon^{-1}} \qquad (3)$$

where $\mathbf{S_a}$ is the uncertainty covariance matrix on the knowledge of the prior state and $\mathbf{S_\varepsilon}$ the error covariance matrix of the forward

220 model and the measurement.

Rodgers, 2000 showed that the trace of $\mathbf{A}$ represents the total degree of freedom for signal (dofs), that gives the number of independent pieces of information provided by the observing system as regards the state vector.

The knowledge of the state vector posterior to the measurement is described by the total error covariance matrix $\mathbf{S_x}$, and can be

225 written as:

$$S_x = S_{smoothing} + S_{meas.} + S_{fwd.mod.} \tag{4}$$

where $S_{smoothing}$ is the smoothing error covariance matrix and describes the vertical sensitivity of the measurements to the retrieved profile, and it is given by:

$$S_{smoothing} = (A - I)S_a(A - I)^T \tag{5}$$

230   $S_{meas.}$ is the contribution of the measurement error covariance S_m associated with spectral noise, and it is written as:

$$S_{meas.} = GS_mG^T \tag{6}$$

$S_{fwd.mod.}$ is the contribution of the forward model error covariance matrix S_f associated with uncertainties from non-retrieved model parameters described by the covariance matrix S_b:

$$S_{fwd.mod.} = GK_bS_b(GK_b)^T = GS_fG^T \tag{7}$$

235   where K_b is the forward model derivative as regards non-retrieved model x_b and S_b is the uncertainty covariance matrix attached to x_b.

3.3.2.1 A priori error covariance matrix

The a priori error covariance matrix S_a is assumed diagonal with the ith diagonal element $(S_{a,ii})$ defined as:

240   $$S_{a,ii} = \sigma_{a,i}^2 \text{ with } \sigma_{a,i} = x_{a,i} \cdot \frac{p_{error}}{100} \tag{8}$$

where $\sigma_{a,i}$ is the standard deviation in the Gaussian statistics formalism. The subscript i represents the ith parameter of the state vector. The prior knowledge of aerosol parameters (D_g, VMR) is supposed to be known with an uncertainty of 100 % (Frankenberg et al., 2012).

3.3.2.2 Measurement error covariance matrix

The measurement error covariance matrix is influenced by the radiometric calibration and the radiometric noise, given by the signal-to-noise ratio (SNR). This error covariance matrix is also assumed to be diagonal, and the ith diagonal element can be computed as follows:

$$S_{m,ii} = \sigma_{m,i}^2 \text{ with } \sigma_{m,i} = \frac{y_i}{SNR} \tag{9}$$

250   where $\sigma_{m,i}$ is the standard deviation of the ith measurement (y_i) of the measurement vector y, representing the noise equivalent spectral radiance. In the case of the IASI instrument the SNR is set to 500.

3.3.2.3 Non-retrieved parameters characterization and accuracy

For the temperature profile and surface temperature, we assumed a realistic uncertainty of 1 K, compatible with the typical values
255   used for the IASI instrument, on each layer of the temperature profile as well as on surface temperature (Pougatchev et al., 2009). The contribution to the ith diagonal element of the forward model error covariance matrix from the jth level temperature can be computed as:

$$\sigma_{f,T_j,i} = \frac{\delta F_i}{\delta T_j} \Delta T \tag{10}$$

where j stands for the jth level and i for the ith measurement.

260   The surface emissivity (ε_s) uncertainty is set to $p_{\varepsilon_s} = 2 \%$, which corresponds to an average value of the albedo absolute accuracy from MODIS and IASI (Capelle et al., 2012), and its contribution to the ith diagonal element of the forward model error covariance matrix is:

$$\sigma_{f,\varepsilon,i} = \frac{\delta F_i}{\delta \varepsilon_s} \Delta \varepsilon_s, \text{ with } \Delta \varepsilon_s = \varepsilon_s \cdot \frac{p_{\varepsilon_s}}{100} \tag{11}$$

Another parameter that was not retrieved is the molecular gas concentration, C_{mol} (in ppm). H_2O is presumed to have an a priori error on the concentration profile of p_{H_2O}=10%. This error value is compatible with the a posteriori uncertainty from IASI Level 2 products given by Clerbaux et al., 2007. The CO_2 uncertainty is set to p_{CO_2} =1% from Engelen and Stephens, 2004 while the O_3 error is p_{O_3} =5% (Boynard et al., 2016). The CH_4 error is estimated to be 5%, which is compatible with the estimation of De Wachter et al., 2017. For the other interfering molecule concentrations (N_2O, cfc-11 and cfc-12), we consider a weak prior knowledge, and their uncertainties are fixed to 100 %.

The prior contribution to the ith diagonal element of the forward model error covariance matrix can be computed as:

$$\sigma_{f,C_{mol},i} = \frac{\delta F_i}{\delta C_{mol}} \Delta C_{mol}, \text{ with } \Delta C_{mol,k} = C_{mol} \cdot \frac{p_{C_{mol}}}{100} \tag{12}$$

The uncertainty percentages are summarized in **Table.1**.

Finally, the total forward model error covariance matrix $\mathbf{S}_f$, assumed diagonal in the present study is given by the sum of all error contributions for each diagonal element, and the ith diagonal element $\mathbf{S}_{f,ii}$ is given by:

$$\mathbf{S}_{f,ii} = \sum_{j=1}^{n_{level}} \sigma_{f,T_j,i}^2 + \sigma_{f,\varepsilon,i}^2 + \sum_{k=1}^{n_{mol}} \sigma_{f,C_{mol,k},i}^2 \tag{13}$$

Here, we did not consider the spectroscopic line parameter, line-mixing, continua or calibration errors.

4 IASI IC analysis: CRI evaluation

In this section, we study the impact of the laboratory CRI measurements to extract information on microphysical aerosol parameters: the geometric diameter D_g and VMR. Accordingly, an IC analysis was performed for the elements of the state vector separately, considering the IASI spectral range between 785 and 1235 cm^{-1}, where mineral dust is detectable. We compute the extinction coefficient (k_{ext}) at 1020 nm adapted from Dubovik et al., 2002 showing that the regression of the optical parameters with 1020 nm are more robust. Subsequently, we derive the VMR at the AOD values interval (0.25 - 1.50) in which IASI is sensitive to dust but also the spectral detection is not close to saturation where we lose the sensitivity to dust parameters, and it is given by:

$$VMR = \frac{AOD}{C_{air} k_{ext} L} \tag{14}$$

where C_{air} is the concentration of the air in the atmospheric profile.

Figure 4 illustrates the dofs and total error from the vector state parameters D_e and VMR separately as function of the AOD and D_e between 1.5 and 5.0 μm . For all CRIs, the dofs is typically greater than 0.50, indicating that the information on mineral dust comes mainly from the measurement **y**. An exception is VZ72 at $D_e = 1.5\ \mu m$, which exhibits the worst case with a $dofs_{VMR}$ is 0.31 for an $AOD = 0.25$. Conversely, the best case is observed for VMA, where the $dofs_{D_e}$is 0.99 for an $AOD = 1.00$. As the AOD increases, the $dofs_{D_e}$ and $dofs_{VMR}$ increase and tend to 1, which indicates that the observation system should adequately provide the necessary information to derive D_e and VMR.

On the other hand, the results suggest that at given D_e, all CRI errors S_{x,D_e} and $S_{x,VMR}$ tend to decrease by 50 % as the AOD increases from 0.25 to 1.50, showing a negative correlation of the total errors with the AOD. For instance, VZ72 errors at $AOD = 0.25$ are $S_{x,D_e} = 0.2$ and $S_{x,VMR} = 0.8$,while $AOD = 1.50$ the errors decrease to $S_{x,D_e} = 10\%$ and $S_{x,VMR} = 40\%$. The relative behavior of the CRIs with increasing D_e drops S_{x,D_e} and $S_{x,VMR}$ by 35%. For example, at $AOD = 1.00$, DB17 errors are $S_{x,D_g} = 12\%$ and $S_{x,VMR} = 37\%$ at $D_e = 1.5\ \mu m$, while these values decrease to $S_{x,D_e} = 8\%$ and $S_{x,VMR} = 25\%$ at $D_e = 5.0\ \mu m$. However, OPAC deviates from this general trend and exhibits an opposite behaviour. While for VMA, no matter the size diameter, its errors remain the least affected. This implies that VMA's errors to changes in particle diameter stay minimal as the diameter grows. Moreover, VZ73 with a close behaviour to DSC22 with S_{x,D_e} of 4% and 5% respectively at $AOD = 1.50$, shows a good

300   compromise that gives low errors regardless of the diameter choice justifying its use so far in the most IR remote sensing applications. DB17 shows an improvement compared to VZ72, consistently with a gain of 30% in sensitivity for all diameters. In conclusion, the different CRIs behaviour's in response to changes in size diameter can vary significantly. Compared to all other datasets, VZ72 exhibits the highest errors, which are primarily attributed to its low spectral resolution, as previously illustrated in **Fig. 3**. The fewer spectral features and structures the CRI possesses, the lower its sensitivity, resulting in higher errors. While most

305   CRIs show an increase in sensitivity with increasing D_e, exceptions like OPAC demonstrate that unique characteristics and behaviours exist within the set. In addition, East Asian dust are transported at low altitudes, hence when the AOD is very high, the thermal contrast between the dust layer and the surface temperatures limits the sensitivity of satellite observations. This is the case of VMA at $D_e = 5.0$ µm, where the errors increase again at $AOD = 1.50$. These results highlight that the selection of an appropriate CRI is crucial in remote sensing retrievals.

5 Solving the inverse problem

310

In this study, instead of using the linear scale, the iterative process is refined by using the logarithmic scale since the order of magnitude can highly vary between the vector state parameters i.e., the diameter value (in µm) is by tenth the order of magnitude of the VMR value (in ppm). This is also the case between the order of magnitude of the vector state **x** and the measurement **y**. The logarithmic scale compresses the range making it easier to analyze trends and patterns, especially in the case of large variation in

315   order of magnitude. The iterative process is then refined by:

$$lnx_{i+1} = lnx_a + \left(\mathbf{K_i^T S_\varepsilon^{-1} K_i + S_a^{-1}}\right)^{-1} \mathbf{K_i^T S_\varepsilon^{-1}} \times [y - F(x_i) + \mathbf{K_i}(lnx_i - lnx_a)] \quad (15)$$

where in this case $\mathbf{K_i} = \delta F/\delta lnx_i$ and $\mathbf{S_a} = \boldsymbol{\sigma_a^2}$ with $\sigma_{a,i} = lnx_a \cdot \frac{perror}{100}$

In this section, the inversion method is used to quantify the microphysical dust parameters (D_e and VMR) and measure the ability of the simulated spectra to reproduce the IASI measurement we calculate the Root Mean Square ($RMS = \sqrt{\Sigma(y_i - F(x_i))^2 / n}$,

320   where n is the number of the spectral channels of 1804). The higher the value of the RMS, the wider is the spread around the IASI spectra and the greater the uncertainty of the spectral fit.

5.1 Application to three spectral pixels

To evaluate the uncertainties of the six refractive indices datasets in reproducing the IASI dust measurements, we applied the inversion process to three observations from the Gobi dust event on 4 May 2017, and calculated the RMS as a measure of

325   uncertainty. We selected spectra with large spectral features, whose simulation presents significant challenges and thereby provides a rigorous test for the CRIs. These observations are distinguished by their contrast in terms of brightness temperature differences $\Delta\mathbf{T_B}$: spectrum 1 at (44.3°N, 119.1°E) with $\Delta\mathbf{T_B} = 2.6$ K, spectrum 2 at (44.0°N, 119.4°E) with $\Delta\mathbf{T_B} = 5.0$ K and spectrum 3 at (49.6 °N, 124.6°E) with $\Delta\mathbf{T_B} = 6.9$ K. **Figure 5** illustrates the spectral fits (in red) from ARAHMIS to IASI observations (in blue) in terms of brightness temperature (in K). A good fit would mean that the model is able to reproduce the observed data with high

330   fidelity, which in turn implies that the model's assumptions and inputs (i.e., atmospheric composition, temperature profiles) are accurate representations of the actual atmospheric conditions. For the spectrum 1, having a small difference in brightness temperature, the simulations yield high precision across all CRIs. This underscores the capability of the atmospheric model and the ARAHMIS code to accurately reproduce the measurements, thereby affirming the reliability of these tools in the case of minimal aerosol concentration. The ability to reproduce the spectral fits decrease for all CRIs while $\Delta\mathbf{T_B}$ increase, nevertheless the

335   extent of this reduction varies across different indices. As $\Delta\mathbf{T_B}$ increases, the spectral fits from VZ72, VZ73, and OPAC exhibit challenges in replicating observations, particularly between 780 and 980 cm⁻¹. Meanwhile, between 1100 and 1230 cm⁻¹, the VZ72

and DB17 fits encounter the most difficulties, whereas VMA fits primarily experience difficulties only between 950 and 980 cm^{-1}. Notably, DSC22 fits exhibit a more robust capability in reproducing observations. By comparing with **Fig. 3**, it becomes evident that CRIs with the highest extinction values within a specific spectral range tend to face greater challenges in reproducing observations accurately within that range. Therefore, the CRIs spectral resolution and features affect the ability to reproduce spectral observations.

We also evaluate the impact of the CRIs on the dust microphysical properties retrieval. D_e and VMR, along with the associated RMS in K and W·m^{-2}·sr^{-1}·(cm^{-1})$^{-1}$, are presented in **Table 2**. Indeed, all datasets demonstrate a rise in RMS values progressing with increasing $\Delta\mathbf{T_B}$, indicating a loss of accuracy between the spectral fits and IASI observations. The DSC22 and VMA datasets exhibit the highest accuracy with the lowest RMS values, followed by DB17 and VZ73, while OPAC and VZ72 show the highest RMS values. In addition, the VMA dataset shows consistency in the RMS values regardless the difference in brightness temperature. Moreover, by increasing $\Delta\mathbf{T_B}$, most datasets exhibit a decreasing trend in the D_e and an increasing trend for VMR values except for DB17. Notably, VMA, DSC22 and VZ73 display the smallest effective diameters in the neighbouring of 3.2 μm, while DB17 shows the highest effective diameters for an average of 5.7 μm.

5.2 Application to the full dust plume

A large dust plume was dispersed between southwest and northeast China within a 2000 km² area in 4 May 2017. We select 1447 IASI dust observations (between 2 and 4 UTC) using the PCA code and study the impact of the six CRIs to retrieve the microphysical parameters using ARAHMIS. **Figure 6** shows the maps of effective diameter, the VMR and the RMS of the fitted spectra. The mean value indicates the range of each parameter, while the standard deviation the degree of dispersion around the mean, offering insight into the variability within each CRI. From 1447 selected observations, the retrieval process had no rejected values. Moreover, it is important to notice that there is a very weak correlation between the RMS and the microphysical parameters D_e and VMR, across different CRIs, which demonstrates that the inversion process does not bias the retrievals. Therefore, the output for the 1447 observations aligns with a gaussian distribution for D_e, VMR and RMS. An example of distribution of D_e, VMR and RMS corresponding for DSC22 dataset is shown in **Fig. 7**, other datasets histograms are found in the **supplementary material**. There is a significant variation of approximately 30% in RMS values, with the highest being for VZ72 and the lowest for DSC22. The optimal mean RMS is 2.1×10^{-3} W·m^{-2}·sr^{-1}·(cm^{-1})$^{-1}$, is associated with the DSC22 and VMA datasets and having a value close to the IASI noise, followed by DB17. DSC22 and DB17 datasets are derived from measurements generated from Gobi Desert samples, while the VMA set is a mixture of pure minerals calculated for the Gobi samples' mineralogy, as previously calculated by Alalam et al. in 2022. When natural dust CRIs are excluded, the most favorable RMS is observed for the VMA dataset, suggesting that a CRI calculated from a pure mineral mixture can be used as a reliable proxy for the natural dust sample CRI. This is consistent with the hypothesis of heterogeneous mixture of pure minerals, as verified by Deschutter, 2022 for the DSC22 sample using the Scanning Electron Microscopy (SEM). Integrating new CRI measurements and the mixing methodology detailed in the mineralogical study by Alalam et al., 2022, has shown the potential to improve the measurements reproduction.

The distribution of retrievals across all plume pixels exhibits a uniform range of magnitude across all CRIs, despite variations in specific values. A factor of 1.6 is observed between the lowest and highest values for the mean effective diameter (lowest in VMA and highest in DB17) and inversely for the VMR. The standard deviation indicates significant variability in these parameters among different CRIs. DSC22 exhibits the largest standard deviation (i.e., variability) for the effective diameter, while VZ73 has the lowest. This contrast highlights the differences in particle size distribution retrieval between these two CRIs. On the other hand, VMA shows the largest distribution width for VMR, therefore a high degree of variability. Conversely, OPAC has the narrowest

distribution, suggesting more uniform VMR values. This analysis reveals different degrees of variability in the effective diameter and VMR across various CRIs.

From a geographical aspect, for all CRIs the spatial distribution displays an increase in diameter from southwest to northeast China. Following the mechanism of the wind front, dust is blown with large diameters northeast particularly from the Horqin Sandy Land

380 and floating dust with smaller diameters from the Gobi Desert. DSC22 has the widest range of effective diameter values. Notably, only VMA and DSC22 show high VMRs in the center of the plume that align with the wind front lines as illustrated by Minamoto et al., 2018.

To validate our results, we didn't find enough ground measurements within the dust plume event that are statistically representative. Nevertheless, two Sun–Sky Radiometer Observation Network (SONET) stations include measurements within the dust plume at

385 the same date and time of the IASI observations: Beijing (40.005; 116.379) and Yanqihu (40.408; 116.674). The size distributions are retrieved using an inversion method as described by Li et al., 2018. In both stations, the mean effective coarse diameter retrieved was of 3.4 μm with a standard deviation of 1 μm. However, it is challenging to compare two different observational and inversion methods in which IASI is a satellite-based instrument measuring the infrared spectrum, while SONET employs ground-based sun-sky radiometers in visible spectrum, therefore different sensitivity to dust detection. Nevertheless, our results show coherent

390 effective size diameters that fall in the range of SONET retrievals, especially the DCS22 dataset, where the mean effective diameter for the overall observations was found to be 3.1 μm with a standard deviation of 1.4 μm.

Finally, through this case study, we have been able to quantify the impact of CRIs on the retrieval of the microphysical parameters (size and concentration) which play a significant role in estimating their radiative effect.

Conclusion and perspectives

395 This study provides valuable insights into the role of dust CRIs in the aerosol microphysical retrievals using infrared remote sensing, in particular IASI detections. It emphasizes the critical importance of selecting the appropriate CRI for accurately determining the microphysical properties of these particles. Initially, we use; the ARAHMIS radiative transfer algorithm to evaluate the IASI measurements sensitivity to various CRIs commonly used in previous studies: VZ72, VZ73, OPAC, DB17, DSC22 and VMA. The information content shows that the IASI measurements is able to accurately retrieve particle size and volume mixing

400 ratio, particularly at higher AOD levels. Moreover, the selection of an appropriate CRI can decrease the total error by 30% which was shown to be the best for the VMA dataset. Hence, improvements in optical properties dust measurements are demonstrated significant potential in aerosol parameter retrieval. This progress is important for future atmospheric studies and applications that rely on CRI laboratory measurements that have higher reliability to satellite spectral observations.

405 The next step, we applied the retrieval process on a dust storm that occurred over China's Gobi Desert on 4 May 2017. By applying the inversion process on three contrasted spectra in terms of brightness temperature difference, VMA and DSC22 showed the most accurate spectral fits to the dust observations. For the overall dust plume results, the microphysical parameters have a uniform distribution across all different indices despite the spread of the values. The spatial distribution of aerosol retrieved parameters was plotted across the East Asian region. The distribution patterns vary for different CRIs, which reflect the influence of CRIs choice

410 on the retrieval. A very weak correlation between RMS and the microphysical properties across different CRIs suggests that the ARAHMIS inversion process is reliable, as it does not produce errors across the range of the retrieved parameters. The results suggest that the accuracy of aerosol property measurements is associated with the source of the dust samples. The optimal mean RMS is linked to datasets derived from specific sources, in this case of the Gobi Desert. In the absence of definitive dust CRIs, the

optical properties of pure mineral aggregates can reliably reflect the regional mineral composition, as shown by low RMS values

415 in such case. This opens the perspectives to better quantify not only the dust mineralogical composition as shown in Alalam et al., 2022, but also, to retrieve more precise microphysical properties through an enhanced understanding of the composition. Understanding the physico-chemical properties of dust more thoroughly is crucial for accurately assessing its radiative effects and its impact on climate and human health.

References

Alalam, P.: Aerosol study using laboratory and IASI measurements: application to East Asian deserts, 2022, https://theses.hal.science/tel-04043142/

Alalam, P., Deschutter, L., Al Choueiry, A., Petitprez, D., and Herbin, H.: Aerosol Mineralogical Study Using Laboratory and 440 IASI Measurements: Application to East Asian Deserts, Remote Sensing 2022, Vol. 14, Page 3422, 14, 3422, https://doi.org/10.3390/RS14143422, 2022.

An, L., Che, H., Xue, M., Zhang, T., Wang, H., Wang, Y., Zhou, C., Zhao, H., Gui, K., Zheng, Y., Sun, T., Liang, Y., Sun, E., Zhang, H., and Zhang, X.: Temporal and spatial variations in sand and dust storm events in East Asia from 2007 to 2016: Relationships with surface conditions and climate change, Science of The Total Environment, 633, 452–462, 445 https://doi.org/10.1016/J.SCITOTENV.2018.03.068, 2018.

Balkanski, Y., Schulz, M., Claquin, T., and Guibert, S.: Reevaluation of Mineral aerosol radiative forcings suggests a better agreement with satellite and AERONET data, Atmos Chem Phys, 7, 81–95, https://doi.org/10.5194/ACP-7-81-2007, 2007.

Di Biagio, C., Formenti, P., Balkanski, Y., Caponi, L., Cazaunau, M., Pangui, E., Journet, E., Nowak, S., Caquineau, S., Andreae O, M., Kandler, K., Saeed, T., Piketh, S., Seibert, D., Williams, E., and Doussin, J. F. C.: Global scale variability of the mineral

450   dust long-wave refractive index: A new dataset of in situ measurements for climate modeling and remote sensing, Atmos Chem Phys, 17, 1901–1929, https://doi.org/10.5194/ACP-17-1901-2017, 2017.

Bi, L., Ding, S., Zong, R., and Yi, B.: Examining Asian dust refractive indices for brightness temperature simulations in the 650–1135 cm−1 spectral range, J Quant Spectrosc Radiat Transf, 247, 106945, https://doi.org/10.1016/J.JQSRT.2020.106945, 2020.

Blumstein, D., Chalon, G., Carlier, T., Buil, C., Hebert, P., Maciaszek, T., Ponce, G., Phulpin, T., Tournier, B., Simeoni, D., Astruc,
455   P., Clauss, A., Kayal, G., and Jegou, R.: IASI instrument: technical overview and measured performances, Infrared Spaceborne Remote Sensing XII, 5543, 196, https://doi.org/10.1117/12.560907, 2004.

Boynard, A., Hurtmans, D., Koukouli, M. E., Goutail, F., Bureau, J., Safieddine, S., Lerot, C., Hadji-Lazaro, J., Wespes, C., Pommereau, J. P., Pazmino, A., Zyrichidou, I., Balis, D., Barbe, A., Mikhailenko, S. N., Loyola, D., Valks, P., Van Roozendael, M., Coheur, P. F., and Clerbaux, C.: Seven years of IASI ozone retrievals from FORLI: Validation with independent total column
460   and vertical profile measurements, Atmos Meas Tech, 9, 4327–4353, https://doi.org/10.5194/AMT-9-4327-2016, 2016.

Capelle, V., Chédin, A., Péquignot, E., Schlüssel, P., Newman, S. M., and Scott, N. A.: Infrared Continental Surface Emissivity Spectra and Skin Temperature Retrieved from IASI Observations over the Tropics, J Appl Meteorol Climatol, 51, 1164–1179, https://doi.org/10.1175/JAMC-D-11-0145.1, 2012.

Capelle, V., Chédin, A., Siméon, M., Tsamalis, C., Pierangelo, C., Pondrom, M., Crevoisier, C., Crepeau, L., and Scott, N. A.:
465   Evaluation of IASI-derived dust aerosol characteristics over the tropical belt, Atmos Chem Phys, 14, 9343–9362, https://doi.org/10.5194/ACP-14-9343-2014, 2014.

Capelle, V., Chédin, A., Pondrom, M., Crevoisier, C., Armante, R., Crepeau, L., and Scott, N. A.: Infrared dust aerosol optical depth retrieved daily from IASI and comparison with AERONET over the period 2007-2016, https://doi.org/10.1016/j.rse.2017.12.008, 2017.

470   Capelle, V., Chédin, A., Pondrom, M., Crevoisier, C., Armante, R., Crepeau, L., and Scott, N. A.: Infrared dust aerosol optical depth retrieved daily from IASI and comparison with AERONET over the period 2007–2016, Remote Sens Environ, 206, 15–32, https://doi.org/10.1016/J.RSE.2017.12.008, 2018.

Chehab, M., Herbin, H., Deguine, A., Gosselin, S., Bizet, V., and Petitprez, D.: First complex refractive indices retrieval from FIR to UV: Application to kaolinite particles, Aerosol Science and Technology, https://doi.org/10.1080/02786826.2024.2318371,
475   2024.

Clarisse, L. and Astoreca, R.: Algorithm Theoretical Basis Document Annex G ULB algorithm for IASI instruments, 2021.

Clarisse, L., Hurtmans, D., Prata, A. J., Karagulian, F., Clerbaux, C., De Mazière, M., and Coheur, P. F.: Retrieving radius, concentration, optical depth, and mass of different types of aerosols from high-resolution infrared nadir spectra, Appl Opt, 49, 3713–3722, https://doi.org/10.1364/AO.49.003713, 2010.

480   Clarisse, L., Clerbaux, C., Franco, B., Hadji-Lazaro, J., Whitburn, S., Kopp, A. K., Hurtmans, D., and Coheur, P.-F.: A Decadal Data Set of Global Atmospheric Dust Retrieved From IASI Satellite Measurements, https://doi.org/10.1029/2018JD029701, 2019.

Clerbaux, C., Hadji-Lazaro, J., Turquety, S., George, M., Coheur, P. F., Hurtmans, D., Wespes, C., Herbin, H., Blumstein, D., Tourniers, B., and Phulpin, T.: The IASI/MetOp1 Mission: First observations and highlights of its potential contribution to GMES2, Space Research Today, 168, 19–24, https://doi.org/10.1016/S0045-8732(07)80046-5, 2007.

485   Crevoisier, C., Clerbaux, C., Guidard, V., Phulpin, T., Armante, R., Barret, B., Camy-Peyret, C., Chaboureau, J. P., Coheur, P. F., Crépeau, L., Dufour, G., Labonnote, L., Lavanant, L., Hadji-Lazaro, J., Herbin, H., Jacquinet-Husson, N., Payan, S., Péquignot, E., Pierangelo, C., Sellitto, P., and Stubenrauch, C.: Towards IASI-New Generation (IASI-NG): Impact of improved spectral resolution and radiometric noise on the retrieval of thermodynamic, chemistry and climate variables, Atmos Meas Tech, 7, 4367–4385, https://doi.org/10.5194/AMT-7-4367-2014, 2014.

490   Cuesta, J., Eremenko, M., Flamant, C., Dufour, G., Laurent, B., Bergametti, G., Höpfner, M., Orphal, J., and Zhou, D.: Three-dimensional distribution of a major desert dust outbreak over East Asia in March 2008 derived from IASI satellite observations, Journal of Geophysical Research: Atmospheres, 120, 7099–7127, https://doi.org/10.1002/2014JD022406, 2015.

Deguine, A., Petitprez, D., Clarisse, L., Deschutter, L., Fontijn, K., and Herbin, H.: Retrieval of refractive indices of ten volcanic ash samples in the infrared, visible and ultraviolet spectral region, J Aerosol Sci, 167, 106100, 495   https://doi.org/10.1016/J.JAEROSCI.2022.106100, 2023.

Deschutter, L.: Propriétés optiques des poussières désertiques de Gobi et de ses composés purs : spectres d'extinction expérimentaux et détermination des indices complexes de réfraction., Université de Lille, 2022.

Desouza-Machado, S. G., Strow, L. L., Imbiriba, B., McCann, K., Hoff, R. M., Hannon, S. E., Martins, J. V., Tanré, D., Deuzé, J. L., Ducos, F., and Torres, O.: Infrared retrievals of dust using AIRS: Comparisons of optical depths and heights derived for a North 500   African dust storm to other collocated EOS A-Train and surface observations, Journal of Geophysical Research Atmospheres, 115, https://doi.org/10.1029/2009JD012842, 2010.

Dubovik, O., Holben, B., Eck, T. F., Smirnov, A., Kaufman, Y. J., King, M. D., Tanré, D., and Slutsker, I.: Variability of Absorption and Optical Properties of Key Aerosol Types Observed in Worldwide Locations, J Atmos Sci, 59, 590–608, https://doi.org/10.1175/1520-0469(2002)059, 2002.

505   Dubovik, O., Herman, M., Holdak, A., Lapyonok, T., Tanré, D., Deuzé, J. L., Ducos, F., Sinyuk, A., and Lopatin, A.: Statistically optimized inversion algorithm for enhanced retrieval of aerosol properties from spectral multi-angle polarimetric satellite observations, Atmos Meas Tech, 4, 975–1018, https://doi.org/10.5194/AMT-4-975-2011, 2011.

Egan, W. G. and Hilgeman, T. W.: Optical properties of inhomogeneous materials : applications to geology, astronomy, chemistry, and engineering, 235, 1979.

510   Engelen, R. J. and Stephens, G. L.: Information content of Infrared Satellite Sounding measurements with respect to CO2, Journal of applied meteorology (1988), 43, 2004.

Frankenberg, C., Hasekamp, O., O'Dell, C., Sanghavi, S., Butz, A., and Worden, J.: Aerosol information content analysis of multi-angle high spectral resolution measurements and its benefit for high accuracy greenhouse gas retrievals, Atmos Meas Tech, 5, 1809–1821, https://doi.org/10.5194/AMT-5-1809-2012, 2012.

14

515   Gibson, E. R., Hudson, P. K., and Grassian, V. H.: Aerosol chemistry and climate: Laboratory studies of the carbonate component of mineral dust and its reaction products, Geophys Res Lett, 33, https://doi.org/10.1029/2006GL026386, 2006.

Glotch, T. D., Rossman, G. R., and Aharonson, O.: Mid-infrared (5–100 μm) reflectance spectra and optical constants of ten phyllosilicate minerals, Icarus, 192, 605–622, https://doi.org/10.1016/J.ICARUS.2007.07.002, 2007.

Herbin, H., Labonnote, L. C., and Dubuisson, P.: Multispectral information from TANSO-FTS instrument – Part 2: Application
520   to aerosol effect on greenhouse gas retrievals, Atmos Meas Tech, 6, 3313–3323, https://doi.org/10.5194/AMT-6-3313-2013, 2013.

Hess, M., Koepke, P., and Schult, I.: Optical properties of aerosols and clouds : The software package OPAC, Bull Am Meteorol Soc, 79, 1998.

Hudson, P. K., Gibson, E. R., Young, M. A., Kleiber, P. D., and Grassian, V. H.: A Newly Designed and Constructed Instrument for Coupled Infrared Extinction and Size Distribution Measurements of Aerosols, Aerosol Science and Technology, 41, 701–710,
525   https://doi.org/10.1080/02786820701408509, 2007.

Journet, E., Balkanski, Y., and Harrison, S. P.: A new data set of soil mineralogy for dust-cycle modeling, Atmos Chem Phys, 14, 3801–3816, https://doi.org/10.5194/ACP-14-3801-2014, 2014.

Klüser, L., Banks, J. R., Martynenko, D., Bergemann, C., Brindley, H. E., and Holzer-Popp, T.: Information content of space-borne hyperspectral infrared observations with respect to mineral dust properties, Remote Sens Environ, 156, 294–309,
530   https://doi.org/10.1016/J.RSE.2014.09.036, 2015.

Kok, J. F., Ridley, D. A., Zhou, Q., Miller, R. L., Zhao, C., Heald, C. L., Ward, D. S., Albani, S., and Haustein, K.: Smaller desert dust cooling effect estimated from analysis of dust size and abundance, Nature Geoscience 2017 10:4, 10, 274–278, https://doi.org/10.1038/ngeo2912, 2017.

Li, Z. Q., Xu, H., Li, K. T., Li, D. H., Xie, Y. S., Li, L., ZHang, Y., Gu, X. F., ZHao, W., Tian, Q. J., Deng, R. R., Su, X. L., Huang,
535   B., Qiao, Y. L., Cui, W. Y., Hu, Y., Gong, C. L., Wang, Y. Q., Wang, X. F., Wang, J. P., Du, W. B., Pan, Z. Q., Li, Z. Z., and Bu, D.: Comprehensive Study of Optical, Physical, Chemical, and Radiative Properties of Total Columnar Atmospheric Aerosols over China: An Overview of Sun–Sky Radiometer Observation Network (SONET) Measurements, Bull Am Meteorol Soc, 99, 739–755, https://doi.org/10.1175/BAMS-D-17-0133.1, 2018.

Masmoudi, M., Chaabane, M., Tanré, D., Gouloup, P., Blarel, L., and Elleuch, F.: Spatial and temporal variability of aerosol: size
540   distribution and optical properties, Atmos Res, 66, 1–19, https://doi.org/10.1016/S0169-8095(02)00174-6, 2003.

Minamoto, Y., Nakamura, K., Wang, M., Kawai, K., Ohara, K., Noda, J., Davaanyam, E., Sugimoto, N., and Kai, K.: Large-scale dust event in East Asia in May 2017: Dust emission and transport from multiple source regions, Scientific Online Letters on the Atmosphere, 14, 33–38, https://doi.org/10.2151/sola.2018-006, 2018.

Peterson, J. T. and Weinman, J. A.: Optical properties of quartz dust particles at infrared wavelengths, JGR, 74, 6947–6952,
545   https://doi.org/10.1029/JC074I028P06947, 1969.

Pierangelo, C., Mishchenko, M., Balkanski, Y., and Chédin, A.: Retrieving the effective radius of Saharan dust coarse mode from AIRS, Geophys Res Lett, 32, 1–4, https://doi.org/10.1029/2005GL023425, 2005.

Pougatchev, N., August, T., Calbet, X., Hultberg, T., Oduleye, O., Schlüssel, P., Stiller, B., St Germain, K., and Bingham, G.: IASI temperature and water vapor retrievals - Error assessment and validation, Atmos Chem Phys, 9, 6453–6458, https://doi.org/10.5194/ACP-9-6453-2009, 2009.

Querry, M. R., Osborne, G., Lies, K., Jordon, R., and Coveney, R. M.: Complex refractive index of limestone in the visible and infrared, Applied Optics, Vol. 17, Issue 3, pp. 353-356, 17, 353–356, https://doi.org/10.1364/AO.17.000353, 1978.

Reed, B. E., Peters, D. M., McPheat, R., Smith, A. J. A., and Grainger, R. G.: Mass extinction spectra and size distribution measurements of quartz and amorphous silica aerosol at 0.33–19 µm compared to modelled extinction using Mie, CDE, and T-matrix theories, J Quant Spectrosc Radiat Transf, 199, 52–65, https://doi.org/10.1016/J.JQSRT.2017.05.011, 2017.

Reed, B. E., Peters, D. M., McPheat, R., and Grainger, R. G.: The Complex Refractive Index of Volcanic Ash Aerosol Retrieved From Spectral Mass Extinction, Journal of Geophysical Research: Atmospheres, 123, 1339–1350, https://doi.org/10.1002/2017JD027362, 2018.

Rodgers, C. D.: Inverse Methods for Atmospheric Sounding, WORLD SCIENTIFIC, https://doi.org/10.1142/3171, 2000.

Ryder, C. L., Highwood, E. J., Walser, A., Seibert, P., Philipp, A., and Weinzierl, B.: Coarse and giant particles are ubiquitous in Saharan dust export regions and are radiatively significant over the Sahara, Atmos Chem Phys, 19, 15353–15376, https://doi.org/10.5194/ACP-19-15353-2019, 2019.

Sokolik, I. N. and Toon, O. B.: Incorporation of mineralogical composition into models of the radiative properties of mineral aerosol from UV to IR wavelengths, J. Geophys. Res.: Atmos., 104, 9423–9444, 1999.

Sokolik, I. N., Toon, O. B., and Bergstrom, R. W.: Modeling the radiative characteristics of airborne mineral aerosols at infrared wavelengths, Journal of Geophysical Research: Atmospheres, 103, 8813–8826, https://doi.org/10.1029/98JD00049, 1998.

Spitzer, W. G. and Kleinman, D. A.: Infrared Lattice Bands of Quartz, Physical Review, 121, 1324, https://doi.org/10.1103/PhysRev.121.1324, 1961.

Vandenbussche, Sophie., Kochenova, S., Vandaele, A. C., Kumps, N., and De Mazière, M.: Retrieval of desert dust aerosol vertical profiles from IASI measurements in the TIR atmospheric window, Atmos Meas Tech, 6, 2577–2591, https://doi.org/10.5194/AMT-6-2577-2013, 2013.

Volz, F. E.: Infrared Refractive Index of Atmospheric Aerosol Substances, Applied Optics, Vol. 11, Issue 4, pp. 755-759, 11, 755–759, https://doi.org/10.1364/AO.11.000755, 1972.

Volz, F. E.: Infrared Optical Constants of Ammonium Sulfate, Sahara Dust, Volcanic Pumice, and Flyash, Applied Optics, Vol. 12, Issue 3, pp. 564-568, 12, 564–568, https://doi.org/10.1364/AO.12.000564, 1973.

De Wachter, E., Kumps, N., Carine Vandaele, A., Langerock, B., and De Mazière, M.: Retrieval and validation of MetOp/IASI methane, Atmos Meas Tech, 10, 4623–4638, https://doi.org/10.5194/AMT-10-4623-2017, 2017.

Yang, P., Feng, Q., Hong, G., Kattawar, G. W., Wiscombe, W. J., Mishchenko, M. I., Dubovik, O., Laszlo, I., and Sokolik, I. N.: Modeling of the scattering and radiative properties of nonspherical dust-like aerosols, Aerosol Science, 38, 995–1014,
580 https://doi.org/10.1016/j.jaerosci.2007.07.001, 2007.

Zheng, J., Zhang, Z., Yu, H., Garnier, A., Song, Q., Wang, C., Di Biagio, C., Kok, J. F., Derimian, Y., and Ryder, C.: Thermal infrared dust optical depth and coarse-mode effective diameter over oceans retrieved from collocated MODIS and CALIOP observations, Atmos Chem Phys, 23, 8271–8304, https://doi.org/10.5194/ACP-23-8271-2023, 2023.

585
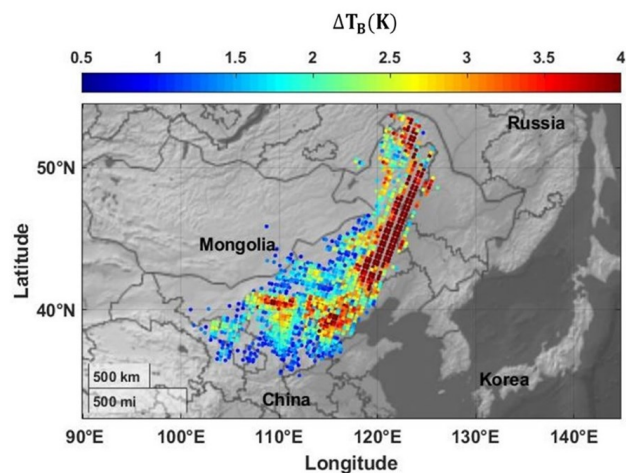
Figure 1. Difference in brightness temperature from IASI dust selection during the dust storm in 4 May 2017 by daylight.
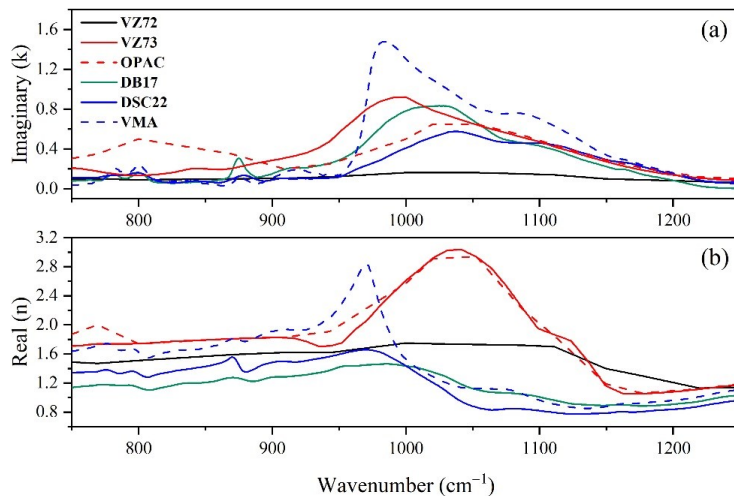
590

Figure 2. Spectral variation of the complex refractive indices of six datasets VZ72: Volz, 1972; VZ73: Volz, 1973; OPAC: Hess et al., 1998; DB17: Di Biagio et al., 2017; DSC22: Deschutter, 2022; VMA: Volume mixing approximation mixture from Deschutter, 2022.
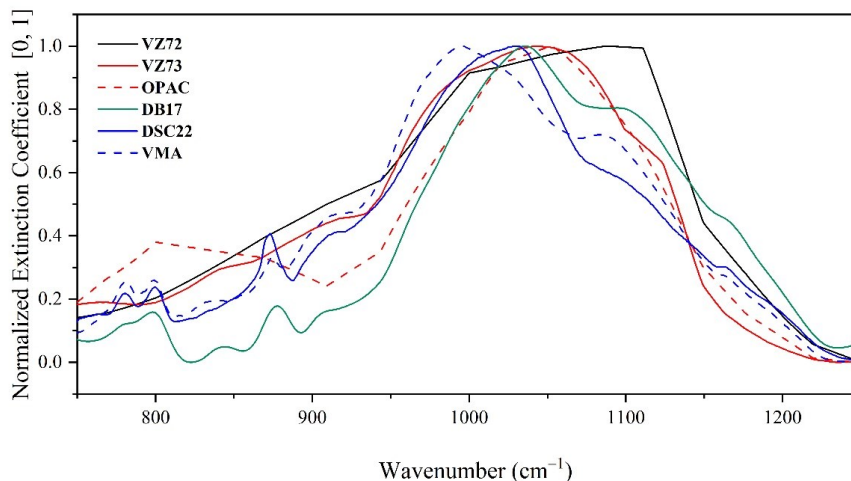
595

Figure 3. Spectral variation of the extinction coefficient using Mie theory of spherical particle of 1 **µm** of diameter on six CRI datasets VZ72: Volz, 1972; VZ73: Volz, 1973; OPAC: Hess et al., 1998; DB17: Di Biagio et al., 2017; DSC22: Deschutter, 2022; VMA: Volume mixing approximation mixture from Deschutter, 2022.

600

Table 1. Non-retrieved parameter a priori and uncertainty references.

Non-retrieved parameters	A priori value reference	A priori uncertainty	Uncertainty reference
H_2O	UWYO database	10%	Clerbaux et al., 2007
CO_2	**CAMS**	1%	Engelen & Stephens, 2004
O_3	**WOUDC database**	5%	Boynard, et al., 2016
CH_4	**CAMS**	5%	De Watcher et al., 2017
N_2O	**Mid-latitude winter standard**	100%	-
CFC-11	**Mid-latitude winter standard**	100%	-
CFC-12	**Mid-latitude winter standard**	100%	-
Surface Temperature	**IASI l2 Product (EUMETSAT)**	1K	Pougatchev et al., 2009
Surface emissivity	**Zhou et al., 2014 + Alalam et al, 2022**	2%	Capelle et al., 2012

605
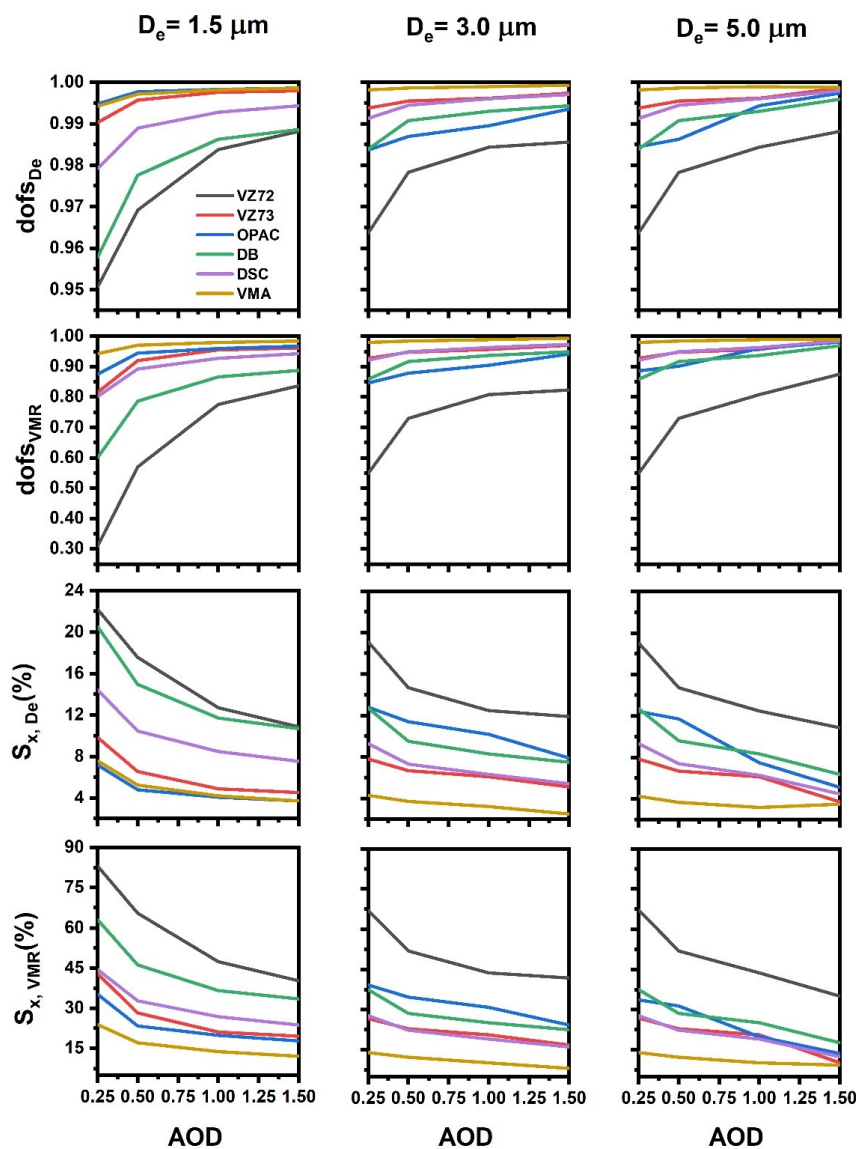
Figure 4. The dofs and total error S_x (in %) of the state vector parameters as function of the AOD for each literature complex refractive index. D_e is the effective particle diameter, and VMR is the volume mixing ratio. VZ72: Volz, 1972; VZ73: Volz, 1973; OPAC: Hess et al., 1998; DB17: Di Biagio et al., 2017; DSC22: Deschutter, 2022; VMA: Volume mixing approximation mixture from Deschutter, 2022.
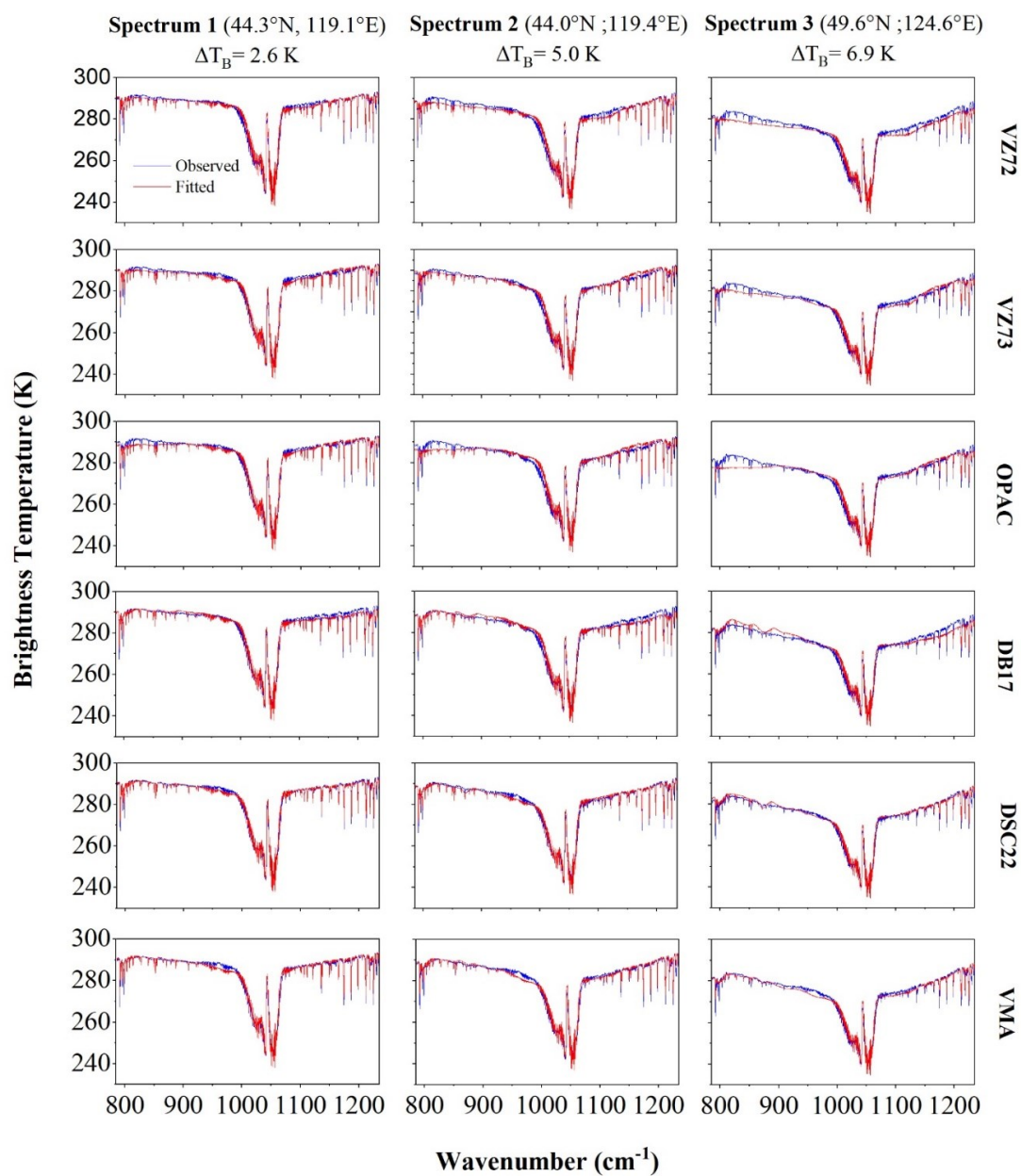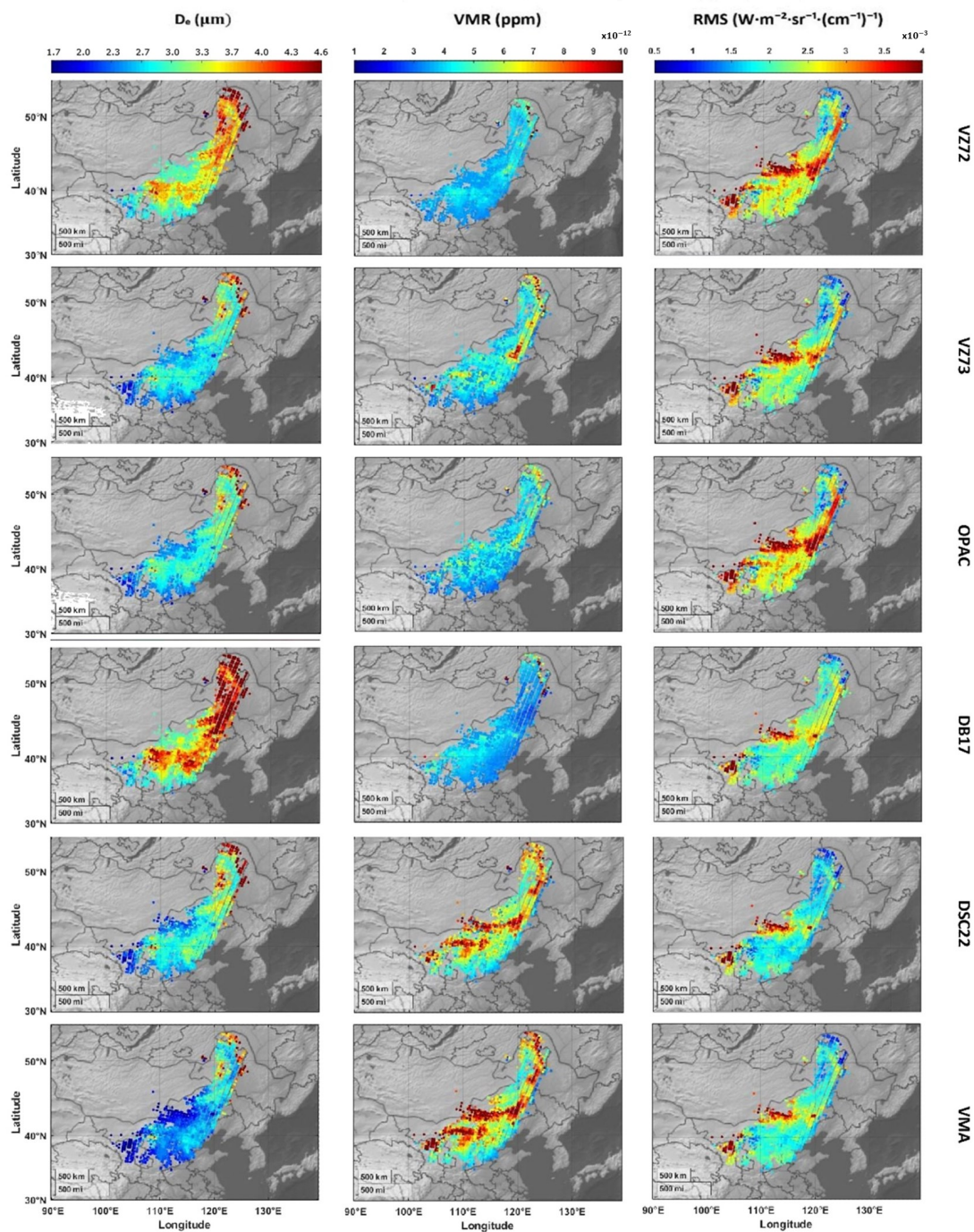
Figure 5. Retrieval of IASI spectral examples from 4 May 2017 using six CRI datasets: VZ72: Volz, 1972; VZ73: Volz, 1973; OPAC: Hess et al., 1998; DB17: Di Biagio et al., 2017; DSC22: Deschutter, 2022; VMA: Volume mixing approximation mixture from Deschutter, 2022.

625 **Table 2.** Retrieved parameters using ARAHMIS applied on three spectra using different CRIs. VZ72: Volz, 1972; VZ73: Volz, 1973; OPAC: Hess et al., 1998; DB17: Di Biagio et al., 2017; DSC22: Deschutter, 2022; VMA: Volume mixing approximation mixture from Deschutter, 2022.

	Spectrum	VZ72	VZ73	OPAC	DB17	DSC22	VMA
Effective diameter	1	4.5	3.6	4.9	4.8	3.4	3.5
	2	4	2.7	4.4	5.1	3.6	2.9
(μm)	3	4.2	3.1	4.3	5.7	2.9	3.1
VMR	1	4.5×10^{-12}	6.0×10^{-12}	5.9×10^{-12}	3.7×10^{-12}	6.5×10^{-12}	6.7×10^{-12}
	2	9.9×10^{-12}	2.6×10^{-11}	1.2×10^{-11}	5.6×10^{-12}	1.0×10^{-12}	2.4×10^{-11}
(in ppm)	3	2.0×10^{-11}	3.0×10^{-11}	3.2×10^{-11}	7.5×10^{-12}	5.1×10^{-11}	3.1×10^{-11}
RMS	1	1.3	1.3	1.4	1.2	0.9	1.2
	2	2.1	1.5	2	1.5	1.1	1.3
(in K)	3	2.3	1.8	2.5	1.8	1.2	1.3
RMS	1	1.6×10^{-3}	1.6×10^{-3}	1.9×10^{-3}	1.5×10^{-3}	1.2×10^{-3}	1.5×10^{-3}
(in	2	2.2×10^{-3}	1.9×10^{-3}	2.6×10^{-3}	1.9×10^{-3}	1.4×10^{-3}	1.6×10^{-3}
W.m^{-2}.sr^{-1}. (cm^{-1})$^{-1}$)	3	2.9×10^{-3}	2.3×10^{-3}	3.2×10^{-3}	2.4×10^{-3}	1.5×10^{-3}	1.6×10^{-3}

Figure 6. Maps of the aerosol microphysical properties ARAHMIS retrieval from the Gobi dust plume event occurred in 4 May 2017. Retrieval from IASI observations is applied on six literature CRIs: VZ72: Volz, 1972; VZ73: Volz, 1973; OPAC: Hess et al., 1998; DB17: Di Biagio et al., 2017; DSC22: Deschutter, 2022; VMA: Volume mixing approximation from Deschutter, 2022.
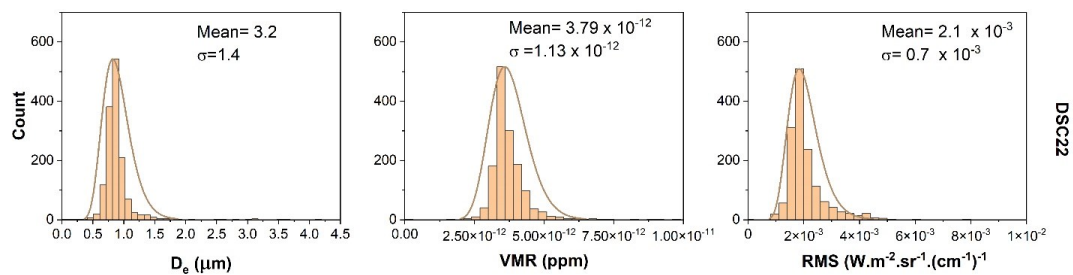
Figure 7. Histograms of the effective diameter, VMR and RMS from ARAHMIS retrieval of the dust plume from 4 May 2017 detected by IASI using DSC22: Deschutter, 2022.

635